Letter Vol. 45, No. 13 / 1 July 2020 / Optics Letters 3373

Waveguide platform for quantum anticentrifugal force

Andrzej Gajewski,[1,†] Daniel Gustaw,[1,†] Nor Roshidah Yusof,[2,†] Norshamsuri Ali,[2] Karolina Słowik,[1] and Piotr Kolenderski[1,*]

[1]Faculty of Physics, Astronomy and Informatics, Nicolaus Copernicus University in Toruń, Grudziadzka 5, 87-100 Torun, Poland
[2]School of Microelectronic Engineering, Universiti Malaysia Perlis, 02000 Arau, Perlis, Malaysia
*Corresponding author: kolenderski@fizyka.umk.pl

Received 12 March 2020; accepted 28 April 2020; posted 5 May 2020 (Doc. ID 392216); published 17 June 2020

This work is a proposition of an experimental platform to observe quantum fictitious anticentrifugal force. We present an analytical and numerical treatment of a rectangular toroidal dielectric waveguide. Solving the Helmholtz equation, we obtain analytical solutions for transverse spatial modes and estimate their number as a function of system characteristics. On top of that, the analysis of the structure is extended onto a real material platform, a thin-film lithium niobate on insulator rib waveguide. The framework presented here can be applied directly to analyze the phenomenon of quantum anticentrifugal force.

https://doi.org/10.1364/OL.392216

Among quantum fictitious forces, the quantum anticentrifugal force (QAF) belongs to the most intriguing. It appears in systems of cylindrical symmetry [1]. Among eigensolutions of the corresponding Schrödinger equation, the subset with a vanishing angular momentum behaves in stark contrast to classical counterparts. A particle described by that solution is attracted towards the center of symmetry rather than pulled away [2,3]. So far, QAF was investigated purely theoretically. However, now capabilities have come into reach to fabricate microscopic geometries in which quantum phenomena are manifested. Experimental methods are mature enough to realize the necessary ingredients such as the phase retrieval algorithm or quantum tomography supported by spatially resolved single photon detection techniques. All of the above bring experiments on QAF into reach. A straightforward platform is based on a bent waveguide (BW) structure [2].

Spatial mode deformation and losses in optical fibers have been analyzed in a variety of cases [4–6], including models assuming toroidal and circular shapes [7], bent slab waveguides [8], bent optical fibers [9], large-area multimode fibers [10], and diffusion waveguides [11,12]. This problem is treated by solving the Helmholtz equation with appropriate boundary conditions. The Helmholtz problem can be solved analytically when it is separable with respect to its variables, which does not hold for all coordinate systems [13]. Another problem is related to geometries with sharp corners, e.g., a rectangular one, which requires approximations such as assumption of strong field confinement in the waveguide [14,15]. With current fabrication techniques, microscaled bending radii can be achieved. Rectangular shapes are typically obtained in the common bottom-up complementary metal-oxide-semiconductor (CMOS) fabrication scheme [16]. These structures have been investigated in the context of spatial mode cross-talk [17] or chromatic dispersion [18].

In this work, we study BW eigenmodes in the context of QAF. Our goal is to identify the modes localized near the inner radius. Such deformation of eigenmodes with respect to their "straight waveguide" counterparts can be understood in analogy to the phenomenon of a fictitious anticentrifugal force acting on a quantum particle in a cylindrically symmetric potential [3]. Modes pushed towards the outer radius of the BW are analogs of quantum particle states with larger angular momenta. To solve the Helmholtz equation we adapt the framework, developed in the context of radio frequency analysis in Refs. [19,20], into the optical domain. The analysis supported by perturbative methods allows us to provide an approximate formula for the number of modes depending on the BW geometry. We discuss example analytical solutions and successfully verify them against solutions obtained by rigorous numerical simulations of full-vectorial Maxwell's equations. A comparison to mode profiles of a realistic rib fiber structure on a substrate is finally provided.

First, we analytically investigate the problem of the propagation of an electromagnetic (EM) wave in a rectangular toroidal dielectric, as shown in Fig. 1(a). It is assumed that the index of refraction in the waveguide n_w is much higher than in its surroundings n_s. A toroidal waveguide has a rectangular profile with dimensions a and b. We assume an interior (exterior) bending radius of r_1 (r_2). We will derive spatial mode profiles of the electric field (EF) $\vec{E}(\vec{r})e^{-i\omega t}$ of an EM wave propagating along the BW. Here, ω is the mode eigenfrequency. We assume the polarization direction of the EF to be parallel to the r axis during the propagation. This is clearly an approximation that however yields solutions in very good agreement with the numerical ones, as we later show. Then, the vectorial notation can be dropped. In order to find $E(\vec{r})$, we solve the Helmholtz equation $\Delta E + (k_{w,s}^2 - 1/r^2)E = 0$, where $k_{w,s} = kn_{w,s}$ is the momentum of the EM field inside (subscript w) or outside (subscript s) the waveguide, and $k = \omega/c$. In cylindrical coordinates (r, ϕ, z), the Helmholtz equation takes the form

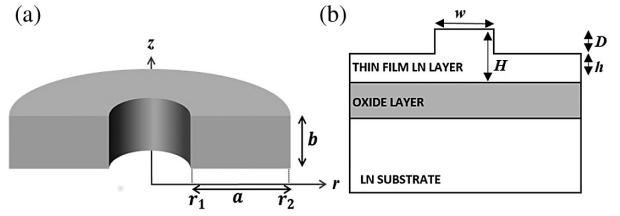

Fig. 1. (a) Rectangular-profile toroidal waveguide geometry. (b) Cross-section view of lithium niobate on insulator rib waveguide with $h = 100$ nm, $D = 500$ nm, and $W = 1000$ nm.

$$\frac{1}{r}\frac{\partial E}{\partial r} + \frac{\partial^2 E}{\partial r^2} + \frac{1}{r^2}\frac{\partial^2 E}{\partial \phi^2} + \frac{\partial^2 E}{\partial z^2} + \left(k_{w,s}^2 - \frac{1}{r^2}\right) E = 0. \quad \textbf{(1)}$$

This choice of coordinate system, along with an assumption of strong confinement, allows one for a variable separation $E(r, \phi, z) = R(r)\Phi(\phi)Z(z)$. Ignoring trivial solutions, we can rewrite Eq. (1) in the following form:

$$\frac{1}{rR}\frac{\partial R}{\partial r} + \frac{1}{R}\frac{\partial^2 R}{\partial r^2} + \frac{1}{r^2\Phi}\frac{\partial^2 \Phi}{\partial \phi^2} + \frac{1}{Z}\frac{\partial^2 Z}{\partial z^2} + k_{w,s}^2 - \frac{1}{r^2} = 0. \quad \textbf{(2)}$$

The independence of variables leads to:

$$\frac{1}{\Phi}\frac{\partial^2 \Phi}{\partial \phi^2} = -m^2, \quad \textbf{(3)}$$

$$\frac{1}{Z}\frac{\partial^2 Z}{\partial z^2} = \begin{cases} -\beta_w^2, & \text{if } |z| < z_0 \\ \beta_s^2, & \text{if } |z| > z_0 \end{cases}, \quad \textbf{(4)}$$

$$\frac{1}{r}\frac{\partial R}{\partial r} + \frac{\partial^2 R}{\partial r^2} + \left(-\frac{m^2+1}{r^2} + h_{w,s}^2\right) R = 0, \quad \textbf{(5)}$$

where m, $\beta_{w,s}$ are positive constants. We assume exponential decay outside the waveguide and oscillating solutions inside. These assumptions lead to a difference in sign on the right-hand side of Eq. (4). For the sake of clarity, we introduce the following definitions: $h_w^2 = k_w^2 - \beta_w^2$, $h_s^2 = k_s^2 + \beta_s^2$, with k_w being the total momentum of the EM field inside the waveguide, β_w – its projection in the z direction, and h_w – the total momentum in the plane perpendicular to the z axis.

Inside the waveguide, h_w is real, resulting in oscillating solutions in the form of a linear combination of Bessel functions along the r axis. Analogously, one obtains oscillating solutions for functions along z and ϕ:

$$\Phi_m(\phi) = C_{1,m}\sin(m\phi) + C_{2,m}\cos(m\phi), \quad \textbf{(6a)}$$

$$Z_{\beta_w}(z) = A_m \sin(\beta_w z) + B_m \cos(\beta_w z), \quad \textbf{(6b)}$$

$$R_{m\beta_w}(r) = \sin(p)J_\alpha(h_w r) + \cos(p)Y_\alpha(h_w r), \quad \textbf{(6c)}$$

where $C_{j,m}$, A_m, B_m, p are real constants, and $\alpha = \sqrt{m^2+1}$. We assume no reflection at the end of the waveguide and consider waves propagating clockwise. Since we assume the EF to be $\hat{r}$ polarized during the propagation, the magnetic field (MF) has components along the z axis and along $\hat{\phi}$. The ignored components scale like r^{-2} and are insignificant in structures of large bending radii compared to the respective wavelength. This polarization allows for perfect confinement of EM wave along the r axis. In our case, the MF is given by $\frac{\partial E}{\partial z}\hat{\phi} - \frac{1}{r}\frac{\partial E}{\partial \phi}\hat{z} = i\omega\vec{B}$. Boundary conditions for MFs and EFs force continuity of $\Phi_m(\phi)$, $R_{m\beta}(r)$, $Z_\beta(z)$, and $Z'_\beta(z)$ on all boundaries. Continuity of the radial component of the EF and the MF leads us to the conclusion that $h_w = h_s = h$, and as a result, $k^2 n_w^2 - \beta_w^2 = k^2 n_s^2 + \beta_s^2$. The explicit form of the boundary conditions reads

$$\pm A_m \sin(\beta_w z_0) + B_m \cos(\beta_w z_0) = (-1)^S e^{-\beta_s z_0}, \quad \textbf{(7a)}$$

$$\beta_w(A_m \cos(\beta_w z_0) \mp B_m \sin(\beta_w z_0)) = \mp(-1)^S e^{-\beta_s z_0}, \quad \textbf{(7b)}$$

$$\sin(p)J_\alpha(hr_q) + \cos(p)Y_\alpha(hr_q) = 0, \quad \textbf{(7c)}$$

where $q = 1, 2$, Eqs. (7a) and (7b) are conditions for the EFs and the MFs, respectively. D_m is a real constant. Solutions with $S = 0$ correspond to even modes, and with $S = 1$ to odd, denoted below with "e"("o").

Let us analyze the boundary condition in the z-axis direction. Since the EF is $\hat{r}$ polarized, the same radial components of the EFs and MFs vanish. This leads to conditions of perfect confinement along the r axis, Eq. (7c). The global phase is unimportant, and we set $D_m = 1$. It follows that

$$[\tan(\beta_w z_0)]^{(-1)^{1-S}} = (-1)^{1-S}\sqrt{k^2(n_w^2 - n_s^2) - \beta_w^2}/\beta_w. \quad \textbf{(8)}$$

The number of roots of the above equations can be estimated as

$$N_o^{\max} = \left\lceil \frac{kb}{2\pi}\sqrt{n_w^2 - n_s^2}\right\rceil_s, \quad N_e^{\max} = \left\lceil \frac{kb}{2\pi}\sqrt{n_w^2 - n_s^2} - \frac{1}{2}\right\rceil, \quad \textbf{(9)}$$

where $\lceil\ \rceil$ is the ceiling function. The boundary conditions result in a discrete set of solutions numbered by N. From now on, we will denote solutions of Eq. (8) by $\beta_i(h_i)$, where $i < N^{\max} = N_e^{\max} + N_o^{\max}$.

We move on to the boundary condition for the EF amplitude in the r-axis direction, which will let us determine the allowed values of the p parameter defined in Eq. (6c). The amplitude has to vanish at r_1 and r_2 resulting in conditions [Eq. (7c)]. For a given m, the condition for existence of non-trivial solutions of Eq. (7c) has the following form:

$$0 = J_\alpha(h_i r_2)Y_\alpha(h_i r_1) - J_\alpha(h_i r_1)Y_\alpha(h_i r_2), \quad \textbf{(10)}$$

with $p_\alpha = \arctan(-Y_\alpha(h_i r_j)/J_\alpha(h_i r_j))$, and $j = 1, 2$. We are going to estimate the number of possible values of m for which the equation above has a solution. A perturbative analysis supplemented by numerical simulations leads us to the upper limit for the mode number:

$$l_i^{\max} = \left\lfloor \sqrt{k^2 n_w^2 - \beta_i^2}(r_2 - r_1)/\pi \right\rfloor. \quad \textbf{(11)}$$

Each of the predicted modes must fulfill an additional condition: $n_s < n_{\text{eff}} < n_w$. To derive Eq. (11), we assume that the field propagating along the waveguide does not decay, and thus m, which might have non-integer values, must be real. The latter point might seem surprising at first glance: in a real waveguide, significant radiation decay is expected due to bending. However,

the assumption of negligible losses follows naturally from the previously made assumption of a large index ratio $n_w/n_s \to \infty$ and the resulting boundary conditions. Since the field vanishes at the side walls of the waveguide, there is almost no energy dissipation into the surroundings.

We now derive formula (11). To solve the Helmholtz Eq. (5), we use a perturbative analysis:

$$-\frac{\partial^2 R}{\partial r^2}+\eta\left(\alpha^2\left(\frac{1}{r^2}-\frac{1}{\bar{r}^2}\right)-\frac{1}{r}\frac{\partial}{\partial r}\right)R=\left(h_i^2-\frac{\alpha^2}{\bar{r}^2}\right)R, \tag{12}$$

where for simplicity we introduce the following notation: $\bar{r}=(r_2+r_1)/2$, $\Delta r=r_2-r_1$ and a perturbative parameter η. Setting $\eta=1$ yields Eq. (5). The zeroth-order equation ($\eta=0$)

$$-\frac{\partial^2 R^0(r)}{\partial r^2}=\left[h_i^2-\left(\frac{\alpha^0}{\bar{r}}\right)^2\right]R^0(r) \tag{13}$$

has the solution: $R^0(r)=\sin[(r-r_1)\sqrt{h_i^2-(\frac{\alpha^0}{\bar{r}})^2}]$, where the argument is chosen to fulfill the boundary condition (7e), with $q=1$. The condition for $q=2$ results in the expression for the number of oscillations: $l\pi=\sqrt{h_i^2-(\alpha^0/\bar{r})^2}\Delta r$. This leads to the zeroth-order relation for the possible values of m:

$$m_{i,l}^0=\bar{r}\sqrt{h_i^2-(l\pi)^2(\Delta r)^{-2}-\bar{r}^{-2}}. \tag{14}$$

In the context of QAF, this parameter corresponds to the angular momentum of a particle subject to a quantum anticentrifugal potential, attractive for small and repulsive for large m. The maximal number of modes $l_i^{\max}$ corresponds to the maximal value of l_i for which $m_{i,l}^0$ is real:

$$h_i>\frac{l_i\pi}{\Delta r}\sqrt{1+\left(\frac{\Delta r}{\bar{r}l_i\pi}\right)^2}\approx\frac{l\pi}{\Delta r}. \tag{15}$$

Thus, we arrive at Eq. (11). The 0th-order approximation $l_i^{\max}$ is not valid for wide structures supporting a large number of radial modes. Including higher perturbation orders only shifts the values of m, but the number of solutions $l^{\max}$ remains constant. The finite number of modes originates from the condition given by Eq. (10), which is a function of m. This can be understood based on the mathematical behavior of the Bessel functions: they change their character from oscillating to exponential when the order m exceeds the value of their argument.

We proceed to discuss example solutions corresponding to a multimode waveguide with $r_1=0.5$ μm, $r_2=1.5$ μm, $b=0.5$ μm, $n_w=2.3$, and $n_s=1$. The spatial mode parameters are computed in accordance to Eq. (9), and Eq. (11) at the free-space wavelength 800 nm, and are given in Table 1. Additionally, the profiles of the straight waveguide modes were obtained by setting $r_{1,2}\to\infty$, as the characteristics of the BW are asymptotically converged under this condition (Figs. 2 and 3). As expected, the straight waveguide supports symmetric mode profiles at fundamental and higher-order modes, as depicted in Figs. 2(a) and 2(b), respectively.

To demonstrate the accuracy and consistency of the spatial profiles given analytically, the same BW was analyzed using COMSOL software. It was simulated in an EM wave

Table 1. Parameters of Spatial Modes for Waveguide Geometry Specified in the Main Text[a]

n	1	2	3
β [μm^{-1}]	5.03	9.94	14.46
h [μm^{-1}]	17.35	15.09	1.08
(m, n_{eff})	$i=1$	$i=2$	$i=3$
$l=1$	(20.54, 2.03)	(17.391, 1.75)	(11.53, 1.22)
$l=2$	(16.50, 1.86)	(13.54, 1.58)	(8.08, *1.04*)
$l=3$	(13.23, 1.69)	(10.41, 1.40)	(4.56, *0.6*)
$l=4$	(10.26, 1.46)	(7.15, *1.02*)	—
$l=5$	(6.03, *0.9*)	—	—

[a]Values of m are based on Eq. (10); values of n_{eff} in italic correspond to nonphysical solution.

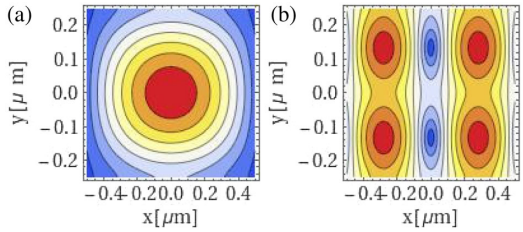

Fig. 2. Straight waveguide modes (a) $(i, l)=(1, 1)$ and (b) $(2, 2)$.

frequency domain by exploiting the finite element method mode solver in cylindrical coordinates. 1 μm thick perfectly matched layers and extremely fine meshing of 50 nm step size were used. Simulations were performed in the module "2.5 D," which assumes axial symmetry, which means we no longer consider a BW but rather a ring with a rectangular cross section. Nevertheless, the propagation equation for such a ring still has the same form as for the BW. The difference lies in an additional boundary condition for the Φ function, which leads to the requirement for m to be an integer. The good agreement between the analytical and numerical solutions [Figs. 3(a) and 3(b)] justifies the analytical model. However, not all modes found analytically could be recreated in simulation. Mode $(i, l)=(2, 3)$ could be found only in the case of the rib waveguide. The BW mode profiles are distorted and shifted towards the sidewalls of the BW [Figs. 3(a) and 3(b)]. The shift is larger for a reduced bending radius. For $r_2=1$ μm, the fundamental mode $(i=l=1)$ is shifted significantly towards the outer wall. As l grows, modes shift towards the inner sidewall (Fig. 3ii–vi). To quantify these observations, we introduce the mode average radial position $r_{\text{av}}(i, l)=\iint|E_{i,l}(r, 0, z)|^2 r\,dr\,dz/\iint|E_{i,l}(r, 0, z)|^2 dr\,dz$. This quantity is computed for each of the modes in Table 1, and the analytical and numerical results are compared in Table 2. For the straight waveguide, the average radial position is always in the center of the waveguide $r_{\text{av}}=1$ μm. On the contrary, $r_{\text{av}}(i, l)$ decreases with increasing mode numbers i and l. This counterintuitive behavior was described in a quantum-optical picture through the notion of QAF [1–3], where in cylindrical geometries, depending on the mode number l, the photons can be directed towards or outwards from the radial axis.

We now extend our analysis to a realistic material platform. We consider a lithium niobate (LN) on insulator (LNOI) due to its production feasibility with low losses within a broad transparency window spanning from $0.5-5$ μm. We have

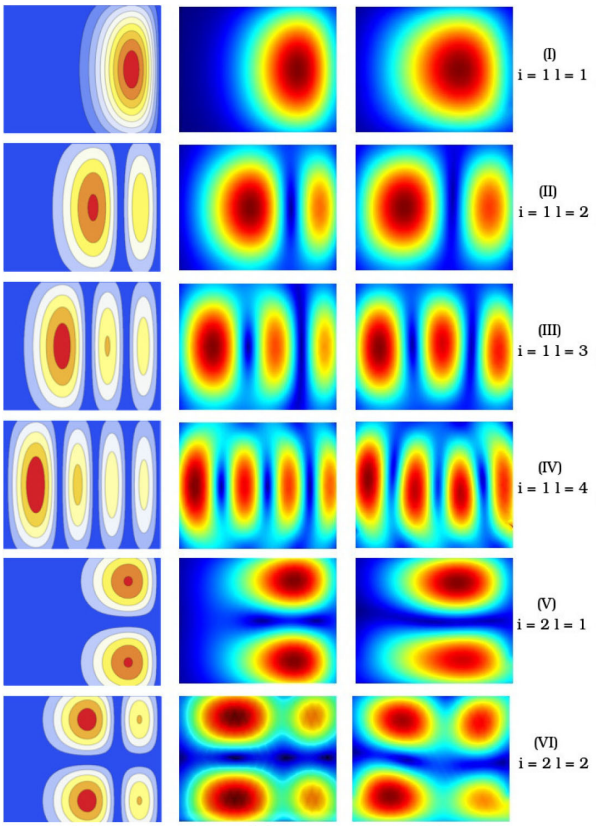

Fig. 3. Spatial modes of BW in Fig. 1. (a) Analytical and (b) numerical solutions to the geometry in Fig. 1(a); (c) modes of the LNOI rib waveguide in Fig. 1(b). Rows i–iv (v–vi) correspond to even (odd) solutions.

Table 2. Average Radial Position of Waveguide Modes Computed Analytically and Numerically[a]

	Average Radial Position r_{av} (μm)								
Mode Number	Analytical (Toroid)			Numerical (Toroid)			Numerical (Rib)		
	$i=1$	$i=2$	$i=3$	$i=1$	$i=2$	$i=3$	$i=1$	$i=2$	$i=3$
$l=1$	1.29	1.27	1.21	1.21	1.17	1.05	1.17	1.12	1.00
$l=2$	1.13	1.09	*0.99*	1.04	0.98	–	0.98	0.99	–
$l=3$	1.00	0.95	*0.9*	0.95	–	–	0.91	1.10	–
$l=4$	0.90	*0.89*	–	0.95	–	–	0.90	–	–

[a]Values in italic correspond to non-physical solutions.

simulated a thin-film LNOI rib waveguide structure deposited on top of 2 μm of buried oxide of 500 μm thick LN substrate, [Fig. 1(b)], with bending radius $r = 10$ μm. The high index contrast between the LN core ($n_{LN} = 2.14$) and a glass cladding ($n_{SiO2} = 1.44$) causes strong confinement across the structure. The eigenmode characteristics result from the effective refractive index $n_{eff} = m/(r_{av}k)$. A propagation mode is obtained when the $n_{SiO2} < n_{eff} < n_{LN}$ condition is fulfilled. The maximum value of n_{eff} corresponds to the fundamental eigenmode. Figure 3(c) depicts spatial profiles of rib waveguide modes. Despite the significantly richer, more realistic and asymmetric waveguide geometry, the modes in Fig. 3(c) show striking similarity to those in Figs. 3(a) and 3(b). Our analytical model correctly predicts all qualitative features including the modal distortion towards/outwards from the center. The slight asymmetry in the z direction is a natural consequence of the symmetry breaking due to the presence of the substrate [oxide layer; Fig. 1(b)].

In summary, we have developed an analytical model for spatial modes in a rectangular BW with a high refraction index. We have juxtaposed that model with accurate numerical solutions for the same geometry, as well as with a feasible experimental platform. The model allows one to predict the spatial mode number and profiles with a good level of accuracy. We have found that the eigenmodes of the investigated structures show an intriguing behavior with their distortion being linked to the mode order l and the curvature of the geometry. Similar equations describe the phenomenon of QAF. Thus, the setups proposed in this work may provide a classical platform to test quantum phenomena in curved geometries [3].

Funding. Fundacja na rzecz Nauki Polskiej (project First Team, Project HEIMaT No. Homing/2016-1/8); Narodowa Agencja Wymiany Akademickiej (PROM Project no. PPI/PRO/2018/1/00016/U/001, TAPS 2019 program); Narodowe Centrum Nauki (NCN Sonata 12 grant no. 2016/23/D/ST2/02064).

Disclosures. The author declares no conflicts of interest.

[†]These authors contributed equally to this work.

REFERENCES

1. M. A. Cirone, K. Rzażewski, W. P. Schleich, F. Straub, and J. A. Wheeler, Phys. Rev. A **65**, 022101 (2001).
2. R. Dandoloff and V. Atanasov, Annalen der Physik **523**, 925 (2011).
3. R. Dandoloff, B. Jensen, and A. Saxena, Phys. Lett. A **378**, 510 (2014).
4. D. Marcuse, J. Opt. Soc. Am. **66**, 311 (1976).
5. E. Snitzer, J. Opt. Soc. Am. **51**, 491 (1961).
6. J. Hu and C. R. Menyuk, Adv. Opt. Photon. **1**, 58 (2009).
7. M. S. Janaki and B. Dasgupta, IEEE T. Plasma. Sci. **18**, 78 (1990).
8. K. Hiremath, M. Hammer, R. Stoffer, L. Prkna, and J. Čtyroký, Opt. Quantum. Electron. **37**, 37 (2005).
9. R. Klepáček and L. Kalvoda, in *Society of Photo-Optical Instrumentation Engineers (SPIE) Conference Series*, vol. **8073** (2011).
10. R. C. G. Smith, A. M. Sarangan, Z. Jiang, and J. R. Marciante, Opt. Express **20**, 4436 (2012).
11. E. M. Conwell, Appl. Phys. Lett. **23**, 328 (1973).
12. G. Nalesso and F. M. Pigozzo, Opt. Commun. **282**, 3596 (2009).
13. P. M. Morse and H. Feshbach, *Methods of Theoretical Physics* (McGraw-Hill Science/Engineering/Math, 1953).
14. L. Marin, D. Lesnic, and V. Mantic, J. Sound Vib. **278**, 39 (2004).
15. L. Marin, Appl. Math. Model. **34**, 1615 (2010).
16. M. Beals, J. Michel, J. Liu, D. Ahn, D. Sparacin, R. Sun, C. Hong, L. Kimerling, A. Pomerene, D. Carothers, J. Beattie, A. Kopa, A. Apsel, M. Rasras, D. Gill, S. Patel, K. Tu, Y. Chen, and A. White, Proc. SPIE **6898**, 689804 (2008).
17. L. H. Gabrielli, D. Liu, S. G. Johnson, and M. Lipson, Nat. Commun. **3**, 1217 (2012).
18. W. Zhang, Q. Zhou, P. Wang, Y. Huang, and J. Peng, in *Society of Photo-Optical Instrumentation Engineers (SPIE) Conference Series*, vol. **8011** (2011).
19. J. A. Cochran and R. G. Pecina, Radio Sci. **1**, 679 (1966).
20. E. Marcatili, Bell Syst. Tech. J. **48**, 2103 (1969).